# Supplementary Information

# Topologically controlled phase transitions and nanoscale film self-assemblies of cage poly(ε-caprolactone) and its counterparts

**Brian J. Ree,[a] Yoshinobu Mato,[b] Li Xiang,[c] Jehan Kim,[d] Takuya Isono,[a] and Toshifumi Satoh[a,*]**

[a]Faculty of Engineering, Hokkaido University, Sapporo 060-8628, Japan
[b]Graduate School of Chemical Sciences and Engineering, Hokkaido University, Sapporo 060-8628, Japan
[c]Department of Chemistry, Pohang University of Science and Technology, Pohang 37673, Republic of Korea
[d]PLS-II Beamline Division, Pohang Accelerator Laboratory, Pohang 37673, Republic of Korea

## Grazing Incidence X-Ray Scattering (GIXS) Data Analysis

The intensity of GIXS ($I_{GIXS}$) from structures in a thin film can be expressed by the following formula:[1-8]

$$I_{GIXS}(\alpha_f, 2\theta_f) \cong \frac{1}{16\pi^2} \cdot \frac{1\text{-}e^{-2\mathrm{Im}(q_z)t}}{2\mathrm{Im}(q_z)} \cdot \begin{bmatrix} |T_i T_f|^2 I_1\left(q_{\parallel}, \mathrm{Re}\left(q_{1,z}\right)\right) + \\ |T_i R_f|^2 I_1\left(q_{\parallel}, \mathrm{Re}\left(q_{2,z}\right)\right) + \\ |T_f R_i|^2 I_1\left(q_{\parallel}, \mathrm{Re}\left(q_{3,z}\right)\right) + \\ |R_i R_f|^2 I_1\left(q_{\parallel}, \mathrm{Re}\left(q_{4,z}\right)\right) \end{bmatrix} \quad (1)$$

where $\alpha_f$ and $2\theta_f$ are the out-of-plane and in-plane exit angle of the out-going X-ray beam respectively,

$\mathrm{Im}(q_z) = |\mathrm{Im}(k_{z,f})| + |\mathrm{Im}(k_{z,i})|$, $\mathrm{Re}(x)$ is the real part of $x$, $t$ is the film thickness, $R_i$ and $T_i$ are the reflected and transmitted amplitudes of the incoming X-ray beam respectively, and $R_f$ and $T_f$ are the reflected and transmitted amplitudes of the outgoing X-ray beam respectively. In addition, $q_{\parallel} = \sqrt{q_x^2 + q_y^2}$, $q_{1,z} = k_{z,f} - k_{z,i}$, $q_{2,z} = -k_{z,f} - k_{z,i}$, $q_{3,z} = k_{z,f} + k_{z,i}$, and $q_{4,z} = -k_{z,f} + k_{z,i}$; here, $k_{z,i}$ is the $z$-component of the wave vector of the incoming X-ray beam, which is given by $k_{z,i} = k_{\circ}\sqrt{n_R^2 - \cos^2 \alpha_i}$, and $k_{z,f}$ is the $z$-component of the wave vector of the outgoing X-ray beam, which is given by $k_{z,f} = k_{\circ}\sqrt{(n_R^2 - \cos^2 \alpha_f)}$, where $k_{\circ} = 2\pi/\lambda$, $\lambda$ is the wavelength of the X-ray beam, $n_R$ is the refractive index of the film given by $n_R = 1 - \delta + i\zeta$ with dispersion $\delta$ and absorption $\zeta$, and $\alpha_i$ is the out-of-plane grazing incident angle of the incoming X-ray beam. $q_x$, $q_y$, and $q_z$ are the components of the scattering vector **q**. $I_1$ is the scattering intensity of the structure in the film, which can be calculated kinematically.

In eq 1, $I_1$ is the scattered intensity from morphological structures in a film and, thus, can be expressed by the following equation:[1-13]

$$I_1(\mathbf{q}) = P(\mathbf{q}) \cdot S(\mathbf{q}) \qquad (2)$$

where $P(\mathbf{q})$ is the form factor that describes the shape, size, and orientation of scatterers in the thin film, and $S(\mathbf{q})$ is the structure factor which provides information on the relative positions of the group of scatterers, such as the crystal lattice parameters, orientation, dimension, and symmetry in an ordered structure and the interdistance of domains.

For the lamellar structure consisted of three layers, the form factor $P(\mathbf{q})$ can be expressed by the following equation:[1,14-16]

$$P(\mathbf{q}) = \left[ \begin{array}{l} 4L_xL_yH_{inner}(\rho_{inner} - \rho_{outer}) \cdot \dfrac{\sin(q_xL_x)}{q_xL_x} \cdot \dfrac{\sin(q_yL_y)}{q_yL_y} \cdot \dfrac{\sin(q_zH_{inner})}{q_zH_{inner}} \; + \\ 4L_xL_yH_{outer}(\rho_{outer} - \rho_{matrix}) \cdot \dfrac{\sin(q_xL_x)}{q_xL_x} \cdot \dfrac{\sin(q_yL_y)}{q_yL_y} \cdot \dfrac{\sin(q_zH_{outer})}{q_zH_{outer}} \end{array} \right]^2 \quad (3)$$

where $L_x$ and $L_y$ are the length and width of lamellar structure respectively, $H_{inner}$ and $H_{outer}$ are the inner and outer layer heights respectively, and $\rho_{inner}$ and $\rho_{outer}$ are the relative electron densities of the inner and outer layers respectively. $\rho_{matrix}$ is the relative electron density of the matrix layer. For the lamellar structure, $H_{inner}$ can be assigned to the layer thickness $l_1$ of phase-1 having a relatively electron density $\rho_{inner}$. The layer thickness $l_2$ of phase-2 (namely, interfacial layer thickness $l_i$) having a relatively electron density $\rho_{outer}$ (= $\rho_i$) can be estimated from $H_{inner}$ and $H_{outer}$: $l_2 = l_i = (H_{outer} - H_{inner})/2$. The third layer thickness $l_3$ having the relatively electron density $\rho_{matrix}$ can be obtained from the long period $D_L$ of lamellar structure that is extracted from the structure factor $S(\mathbf{q})$: $l_3 = (D_L - l_1 - 2l_2)$.

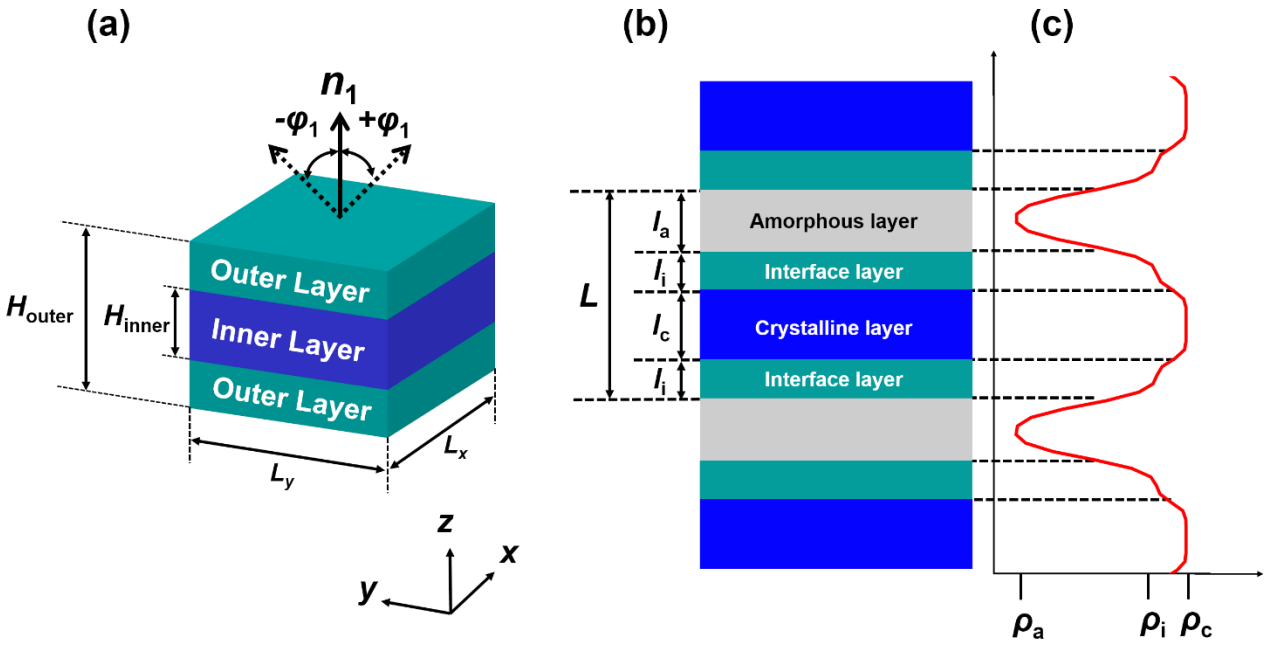


**Fig. S1** The schematic representation of a lamellar structure model consisting three layers: (a) three-dimensional model where $\varphi_1$ is the polar angle (i.e., orientational angle) between the orientational vector $\boldsymbol{n}_1$ parallel to the axis of the long period of lamellar structure and the out-of-plane direction of the film; (b) the front view of lamellar structure model; (c) the electron density profile through the layers

of a lamellar structure where $\rho_c$ is the electron density of crystalline layer and $\rho_a$ is the electron density of amorphous layer.

For the form factor, all structural parameters can be further assumed to follow a Gaussian distribution *G(A)*:

$$G(A) = \frac{1}{\sqrt{2\pi}\sigma_A}\exp\left[-\frac{(A-\overline{A})^2}{2{\sigma_A}^2}\right] \tag{4}$$

where *A* can be one of the parameters, $\overline{A}$ is the mean value, and $\sigma_A$ is the standard deviation of *A* from $\overline{A}$.

For a paracrystalline lattice consisting of the three layers described above, the structure factor $S(\mathbf{q})$ (the so-called interference function or lattice factor) can be determined from the Fourier transform of a complete set of lattice points.[4-8,16-19] In a paracrystal with distortion of the second kind, the positions of the lattice points can only be described with a positional distribution function (i.e., *g*-factor). In the simple case where the autocorrelation function of the crystal lattice is given by the convolution product of the distributions of the lattice points along three axes, and the distribution function is a Gaussian, $S(\mathbf{q})$ can be expressed by the following equation:[16,17]

$$S(\mathbf{q}) = \prod_{k=1}^{3} Z_k(\mathbf{q}) \tag{5}$$

$$Z_k(\mathbf{q}) = 1 + \frac{F_k(\mathbf{q})}{1 - F_k(\mathbf{q})} + \frac{F_k^*(\mathbf{q})}{1 - F_k^*(\mathbf{q})} \tag{6}$$

$$F_k(\mathbf{q}) = |F_k(\mathbf{q})|e^{-i\mathbf{q}\cdot\mathbf{a}_k} \tag{7}$$

$$|F_k(\mathbf{q})| = \exp\left[-\tfrac{1}{2}(q_1^2g_1^2 + q_2^2g_2^2 + q_3^2g_3^2)\right]. \tag{8}$$

Here $g_1$, $g_2$, and $g_3$ (= $g$) are the components of the *g*-factor defined as

$$g_1 = \Delta \mathbf{a_1}/\mathbf{a_1} \tag{9}$$

$$g_2 = \Delta \mathbf{a_2}/\mathbf{a_2} \tag{10}$$

$$g_3 = \Delta \mathbf{a_3}/\mathbf{a_3} \tag{11}$$

where $\mathbf{a_k}$ is the component of the fundamental vector $\mathbf{a}$ of the domain structure and $\Delta\mathbf{a_k}$ is the displacement of the vector $\mathbf{a_k}$. And $q_1$, $q_2$, and $q_3$ are the components of the scattering vector $\mathbf{q}$.

For the lamellar structure composed of three layers, the components of $\mathbf{q}$ in equation 8 are defined by

$$q_1 = \mathbf{a_1} \cdot q_x = \left| d_x \times q_x \right| \tag{12a}$$

$$q_2 = \mathbf{a_2} \cdot q_y = \left| d_y \times q_y \right| \tag{12a}$$

$$q_3 = \mathbf{a_3} \cdot q_z = \left| D_L \times q_z \right| \tag{12a}$$

where $d_x$ and $d_y$ are the lattice dimension parameters (i.e., $d$-spacing values) along the $q_x$- and $q_y$-direction respectively, and $D_L$ is the long period $L$ along the $q_z$-direction.

Moreover, for a structure with a given orientation in a film, its fundamental vectors can be rotated and transformed by a rotation matrix. When the structure of the film is randomly oriented in the plane of the film but uniaxially oriented out of plane, the peak position vector $\mathbf{q_c}$ of a certain reciprocal lattice point $\mathbf{c}^*$ in the sample reciprocal lattice is given by

$$\begin{aligned} \mathbf{q_c} &= \mathbf{R} \cdot \mathbf{c}^* \\ q_c &\equiv \left( q_{c,x}, q_{c,y}, q_{c,z} \right) \end{aligned} \tag{13}$$

where $\mathbf{R}$ is a $3 \times 3$ matrix to decide the preferred orientation of the structure in the film, and $q_{c,x}$, $q_{c,y}$ , and $q_{c,z}$ are the $x$, $y$, $z$ components of the peak position vector $\mathbf{q_c}$, respectively. Using equation 13, every peak position can be obtained. Because of cylindrical symmetry, the Debye-Scherrer ring

composed of the in-plane randomly oriented **c**$^*$ cuts an Ewald sphere at two positions in its top hemisphere: $q_{\parallel} = q_{c,\parallel} \equiv \pm\sqrt{q_{c,x}^2 + q_{c,y}^2}$ with $q_z = q_{c,z}$. Thus diffraction patterns with cylindrical symmetry are easily calculated in the **q**-space. It is then convenient to determine the preferred orientation of known structures and further to analyze anisotropic X-ray scattering patterns. However, since **q**-space is distorted in GIXS by refraction and reflection effects, the relation between the detector plane expressed as the Cartesian coordinate defined by two perpendicular axes (i.e., by $2\theta_f$ and $\alpha_f$) and the reciprocal lattice points is needed. The two wave vectors $k_{z,i}$ and $k_{z,f}$ are corrected for refraction as $k_{z,i} = k_\circ\sqrt{n_R^2 - \cos^2\alpha_i}$ and $k_{z,f} = k_\circ\sqrt{(n_R^2 - \cos^2\alpha_f)}$ respectively. Therefore, the two sets of diffractions that result from the incoming and outgoing X-ray beams, and denoted by $q_1$ and $q_3$ respectively, are given at the exit angles by the following expression:

$$\alpha_f = \arccos\left(\sqrt{n_R^2 - \left(\frac{q_{c,z}}{k_\circ} \pm \sqrt{n_R^2 - \cos^2\alpha_i}\right)^2}\right) \qquad (14)$$

where $q_{c,z}/k_o > \sqrt{n_R^2 - \cos^2\alpha_i}$. In equation 16, the positive sign denotes diffractions produced by the outgoing X-ray beam, and the negative sign denotes diffractions produced by the incoming X-ray beam. The in-plane incidence angle $2\theta_i$ is usually zero, so the in-plane exit angle $2\theta_f$ can be expressed as follow:

$$2\theta_f = \arccos\left[\frac{\cos^2\alpha_i + \cos^2\alpha_f - \left(\frac{q_{c,\parallel}}{k_\circ}\right)^2}{2\cos\alpha_i\cos\alpha_f}\right]. \qquad (15)$$

Therefore, diffraction spots detected on the detector plane in GIXS measurements can be directly compared to those derived using equations 13-15 from an appropriate model and thus analyzed in terms of the model.

To obtain information on the orientation of the paracrystal lattice of the phase separated micro domain structures from GIXS data, the distribution of the orientation vector ***n*** is given by a function $D(\varphi)$, where $\varphi$ is the polar angle between the ***n*** vector and the out-of-plane of the film; for example, $\varphi$ is zero when the ***n*** vector in the film is oriented normal to the film plane (see examples in Figures S1a and S2a). To calculate the 2D GIXS patterns, $D(\varphi)$ should be represented by a numerical function. In relation to the distribution of the lattice orientation, $D(\varphi)$ can generally be considered as a Gaussian distribution:

$$D(\varphi) = \frac{1}{\sqrt{2\pi}\sigma_{\varphi}} \exp\left[-\frac{(\varphi - \bar{\varphi})^2}{2{\sigma_{\varphi}}^2}\right] \tag{16}$$

where $\bar{\varphi}$ and $\sigma_{\varphi}$ are the mean angle and standard deviation of $\varphi$ from $\bar{\varphi}$, respectively. The observed scattering intensity $I_{\mathrm{GIXS},\varphi}(\mathbf{q})$ is obtained by integrating $I_{\mathrm{GIXS}}(\mathbf{q})$ over possible orientations of the lattice:

$$I_{\mathrm{GIXS},\varphi}(\mathbf{q}) = \int_{-\pi}^{\pi} I_{\mathrm{GIXS}}(\mathbf{q}) D(\varphi) \mathrm{d}\varphi \,. \tag{17}$$

The second order orientation factor $O_s$ can be defined as the following equation:[13,16-20]

$$O_s = \int D(\varphi) \frac{(3\cos^2\varphi - 1)}{2} \mathrm{d}\varphi \,. \tag{18}$$

When $D(\varphi)$ is strongly peaked around $\varphi = 0°$ (i.e. vertical alignment), $\cos\varphi = 1$ and $O_s = 1$. On the other hand, when $\varphi = 90°$, $\cos\varphi = 0$ and $O_s = -0.5$. If the orientation is entirely random, $\langle\cos^2\varphi\rangle = 1/3$ and $O_s = 0$. Thus, $O_s$ is a measure of the orientation of nanostructures.

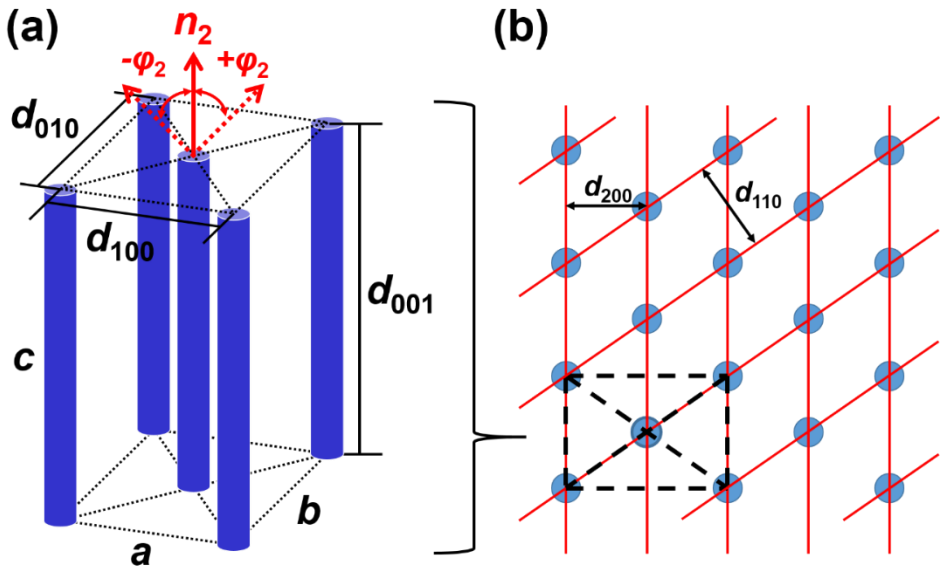


**Fig. S2** The schematic representation of an orthorhombic unit cell composed of molecular cylinders: (a) three-dimensional orthorhombic lattice where $\varphi_2$ is the polar angle (i.e., orientational angle) between the orientational vector $\boldsymbol{n_2}$ parallel to the c-axis of the lattice and the out-of-plane direction of the film; (b) the top view of orthorhombic lattice.

## Synthesis

In this study, all topological poly($\varepsilon$-caprolactone)s were synthesized in accordance to the previously reported method.[21] To compare the specific topological effect, the molecular weight for each arm was fixed to be 3,000 approximately.

**Materials.** Grubbs' catalyst 3rd generation (G3)[21] and 5-(hydroxymethyl)-2,2,5-trimethyl-1,3-dioxane (HTMD)[22] were prepared according to previously reported method. Amberlyst® A21 (Organo Co., Ltd), *N*,*N*-dimethyl-4-aminopyridine (DMAP; Tokyo Chemical Industry Co., Ltd. (TCI), >99.0%), 1-ethyl-3-(3-(dimethylamino)-propyl)carbodiimide hydrochloride (EDC; TCI, >98.0%), ethyl vinyl ether (TCI, >98.0%), and (±)-*exo*-5-norbornenecarboxylic acid (*exo*-NB-COOH; Aldrich, 97%) were used as received. ε-Caprolactone (ε-CL; TCI, >99%) was purified by distillation over $CaH_2$ under reduced pressure and stored in the glovebox. Diphenyl phosphate (DPP; TCI, >99.0%), 2,2-diethyl-1,3-propanol (TCI, >98.0%), and trimethylolpropane (TCI, >98.0%) were purified by azeotropic distillation with dry toluene and stored in the glovebox.

**Instruments.** The polymerization procedures were carried out inside a MBRAUN UNIlab Plus

stainless steel glovebox equipped with a gas purification system (molecular sieves and copper catalyst) in a dry argon atmosphere ($H_2O$, $O_2$ < 0.1 ppm) (MBRAUN Inc., Stratham, NH 03885, USA). The moisture and oxygen levels inside the glovebox were monitored by a moisture sensor (MB-MO-SE 1, MBRAUN Inc.) and an oxygen sensor (MB-OX-SE 1, MBRAUN Inc.), respectively. Dry toluene ( > 99.5%; water content, < 0.001%, Kanto Chemical Co., Inc.) used in the polymerization was purified by passing through a solvent purification system (MB SPS Compact, MBRAUN Inc.) consisting of a column of activated alumina and a column with activated copper catalyst.

The preparative SEC for Grubbs' catalyst removal was performed at 25 °C in $CH_3Cl$ (flow rate, 3.5 mL $min^{-1}$) using a JAI LC-9201 liquid chromatography system (JAI BG-12 degasser, JAI PI-50 pump, JAI RI-50S RI detector, Japan Analytical Industry Co. Ltd. (JAI), Tokyo, Japan) equipped with a JAIGEL-H-P guard column (8 mm × 40 mm, JAI), and a Shodex K-2004 column (linear, 20.0 mm × 300 mm; exclusion limit, 1.4 × 104; particle size, 7 μm, Showa Denko K. K., Tokyo, Japan).

The proton nuclear magnetic resonance ($^1$H NMR) spectra were measured using a JEOL NMR spectrometer (JNM-ECS400, 400 MHz, JEOL Ltd., Tokyo, Japan) using $CDCl_3$ as solvent.

The size exclusion chromatography (SEC) measurements were obtained at 40 °C in THF (flow rate, 1.0 mL $min^{-1}$) using a Shodex GPC-101 gel permeation chromatography system (Shodex DU-2130 dual pump, Shodex RI-71-S reflective index detector, and Shodex ERC-3125SN degasser, Showa Denko K. K., Tokyo, Japan) equipped with a Shodex KF-G guard column (4.6 mm × 10 mm; particle size, 8 μm) and two Shodex KF-804L columns (linear, 8 mm × 300 mm) (Showa Denko K. K., Tokyo, Japan). The SEC system was calibrated with polystyrene (PSt) standards.

**Synthesis of *l*-PCL$_{6k}$.** A typical procedure for the polymerization is as follows (Method A: Scheme S1). Under an argon atmosphere, DPP (4.70 mg, 18.8 μmol) was added to the mixture of *ε*-CL (3.00 g, 26.3 mmol) and 2,2-diethyl-1,3-propanediol (39.1 mg, 375 μmol). The reaction mixture was stirred at 80 °C for 250 min. The polymerization was quenched by the addition of Amberlyst® A21. The polymer crude was purified by the reprecipitation from $CH_2Cl_2$ into cold methanol to give ***l*-PCL$_{6k}$-**

**OH** as a white solid. Yield: 70.3%. $^1$H NMR (400 MHz, $CDCl_3$): $\delta$ (ppm) 4.13-4.01 (m, -OCO($CH_2$)$_4$C$H_2$-), 3.88 (s, ($CH_3CH_2$)$_2$C(C$H_2$O-)$_2$), 3.65 (q, $J$ = 6.4, -C$H_2$OH), 2.38-2.30 (m, -OCOC$H_2$($CH_2$)$_4$-), 1.75-1.54 (m, -OCOC$H_2$C$H_2$($CH_2$)$_3$-, -OCO($CH_2$)$_3$C$H_2$C$H_2$-), 1.45-1.32 (-OCO($CH_2$)$_2$C$H_2$($CH_2$)$_2$-, -C$H_2$C$H_3$), 0.97 (s, -$CH_2$C$H_3$) (Figure S3). $M_{n,NMR}$ = 5,350 g mol$^{-1}$; $M_{n,SEC}$ = 9,590 g mol$^{-1}$; $Đ$ = 1.04 (Figure S4).

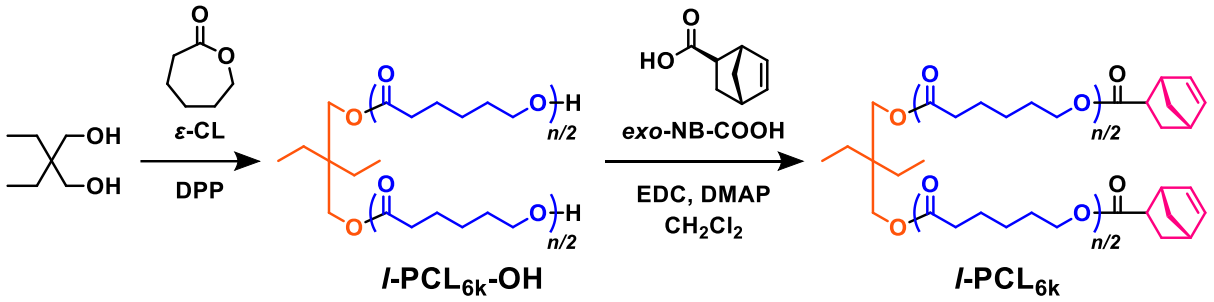


**Scheme S1.** The synthesis of *l*-PCL$_{6k}$, which is a lineal PCL based on one jointing point and two end groups capped with *exo*-NB-COOH.

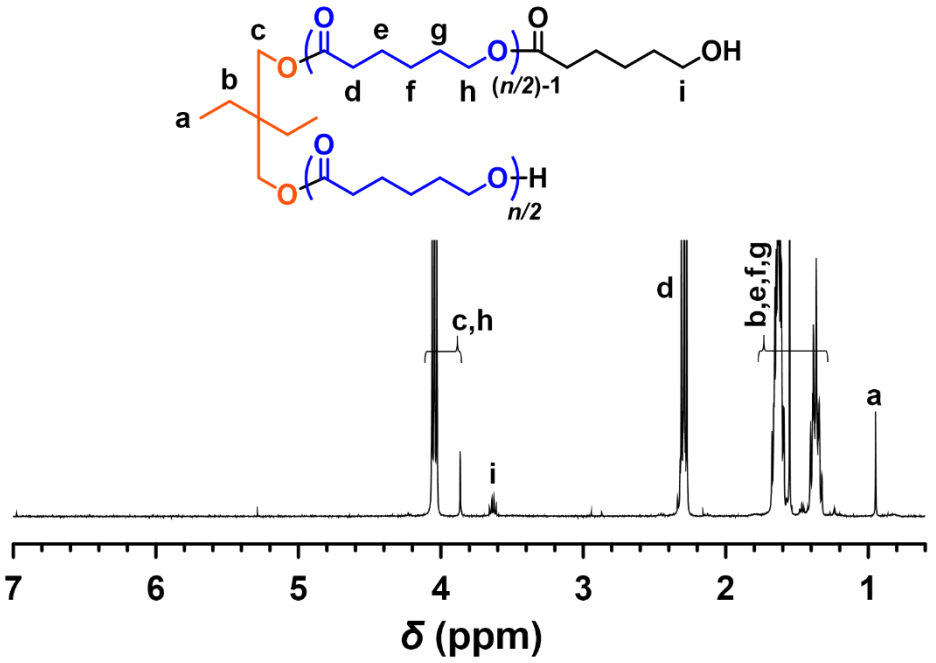


**Fig. S3** $^1$H NMR spectra of ***l*-PCL$_{6k}$-OH** in $CDCl_3$.

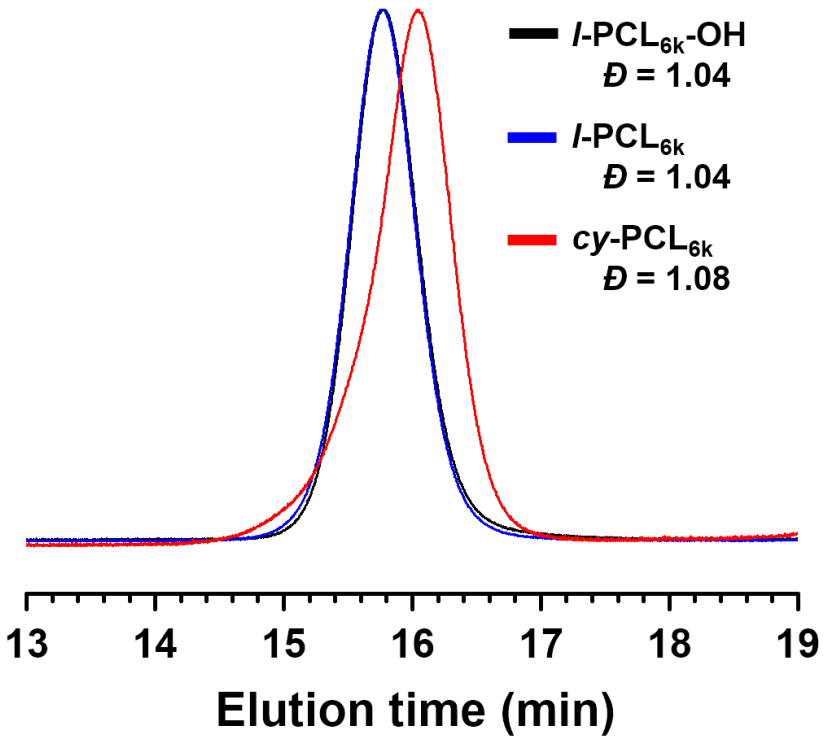


**Fig. S4** SEC traces of ***l*-PCL$_{6k}$-OH** (black), ***l*-PCL$_{6k}$** (blue), and ***cy*-PCL$_{6k}$** (red) in THF (RI detection; eluent, THF; flow rate, 1.0 mL min$^{-1}$; PSt standard).

The obtained ***l*-PCL$_{6k}$-OH** was subjected to $\omega$-end functionalization via a typical procedure for the condensation reaction as follows (Method B; Scheme S1): In a Schlenk flask, ***l*-PCL$_{6k}$-OH** (1.20 g, 224 μmol), *exo*-NB-COOH (126 mg, 912 μmol), DMAP (164 mg, 1.34 mmol), and EDC (258 mg, 1.35 mmol) were dissolved in $CH_2Cl_2$ (12 mL) and the mixture was stirred at r.t. for 24 h. The crude product was purified by reprecipitation from $CH_2Cl_2$ into cold methanol to give ***l*-PCL$_{6k}$** as a white solid. Yield: 59.2%. $^1$H NMR (400 MHz, $CDCl_3$): $\delta$ (ppm) 6.12 (m, -C*H*=C*H*- in norbornene ring), 4.12-4.02 (m, -OCO($CH_2$)$_4$C*H*$_2$-), 3.88 (s, ($CH_3CH_2$)$_2$C(C*H*$_2$O-)$_2$), 3.03 (s, -C*H*-CH-COO- in norbornene ring), 2.92 (s, -C*H*-$CH_2$-CH-COO- in norbornene ring), 2.38-2.26 (m, -OCOC*H*$_2$($CH_2$)$_4$-), 2.21 (m, -$CH_2$-C*H*-COO-), 1.91 (m, *exo*-C*H*- of -CH-C*H*$_2$-CH-COO- in norbornene ring), 1.76-1.53 (m, -OCOC$H_2$C*H*$_2$($CH_2$)$_3$-, -OCO($CH_2$)$_3$C*H*$_2$C$H_2$-), 1.46-1.32 (m, $CH_3$C*H*$_2$-, -OCO($CH_2$)$_2$C*H*$_2$($CH_2$)$_2$-, bridge head -$CH_2$- in norbornene ring, *endo*-C*H*- of -CH-C*H*$_2$-CH-COO-), 0.97 (s, C*H*$_3$C$H_2$-) (Figure S5). $M_{n,NMR}$ = 6,540 g mol$^{-1}$; $M_{n,SEC}$ = 9,770 g mol$^{-1}$; $Đ$ = 1.04 (Figure S4).

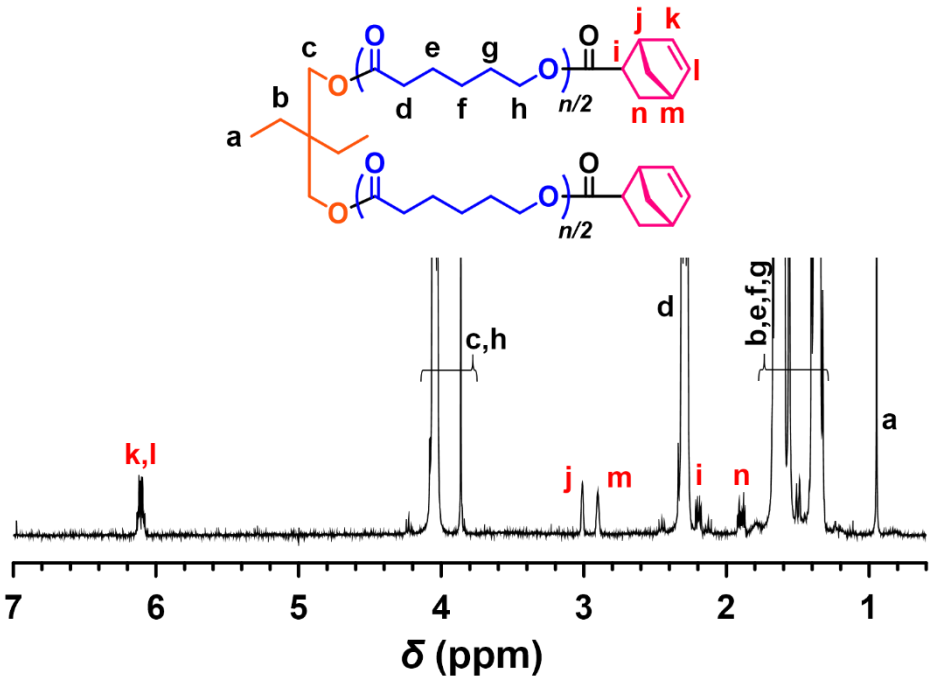


**Fig. S5** $^{1}$H NMR spectra of ***l*-PCL$_{6k}$** in $CDCl_3$.

**Synthesis of *cy*-PCL$_{6k}$.** A typical procedure for the intramolecular consecutive cyclization is as follows (Method C; Scheme S2); G3 (81.2 mg, 91.8 μmol) was added to a three-necked flask and dissolved in deggased-$CH_2Cl_2$ (764 mL). Then, a solution of ***l*-PCL$_{6k}$** ($M_{n,NMR}$ = 6,540 g mol$^{-1}$, 110 mg, 16.8 μmol, 170 μM in $CH_2Cl_2$) was added dropwise to the G3 solution through the additional funnel. After 5 min, the reaction was quenched by the addition of excess amount of ethyl vinyl ether. The metal residue and intermolecularly-reacted impurities in the crude product was removed simultaneously by preparative SEC (solvent, $CHCl_3$) to give ***cy*-PCL$_{6k}$** as a pale brown solid. Yield: 65.5%. $^{1}$H NMR (400 MHz, $CDCl_3$): $\delta$ (ppm) 6.49-4.88 (br, alkenyl of poly(norbornene) backbone), 4.17-3.93 (m, -OCO($CH_2$)$_4$C$H_2$-), 3.88 (s, ($CH_3CH_2$)$_2$C(C$H_2$O-)$_2$), 3.01-1.12 (br, cyclopentane ring of poly(norbornene) backbone), 2.41-2.25 (m, -OCOC$H_2$($CH_2$)$_4$-), 1.85-1.50 (m, -OCOCH$_2$C$H_2$($CH_2$)$_3$-, -OCO($CH_2$)$_3$C$H_2$C$H_2$-), 1.45-1.30 (m, $CH_3$C$H_2$-, -OCO($CH_2$)$_2$C$H_2$($CH_2$)$_2$-), 0.97 (s, C$H_3$CH$_2$-) (Figure S6). $M_{n,SEC}$ = 8,510 g mol$^{-1}$; $Đ$ = 1.08 (Figure S4).

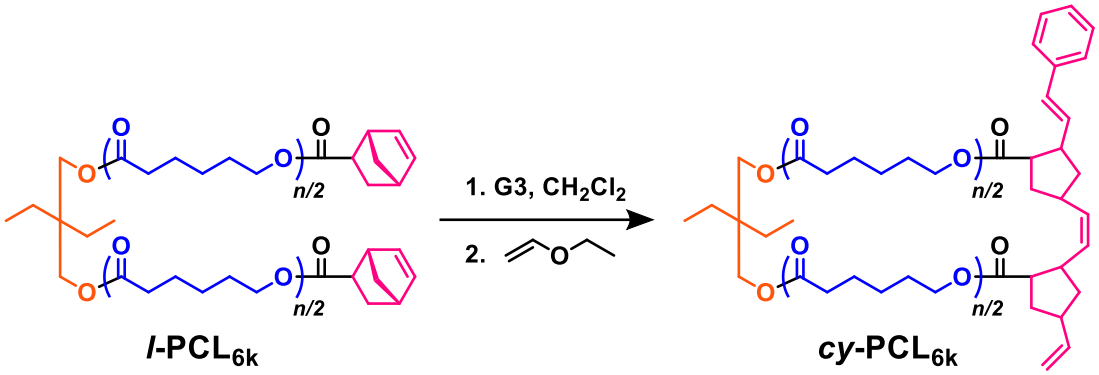


**Scheme S2.** The synthesis of *cy*-PCL$_{6k}$ from *l*-PCL$_{6k}$.

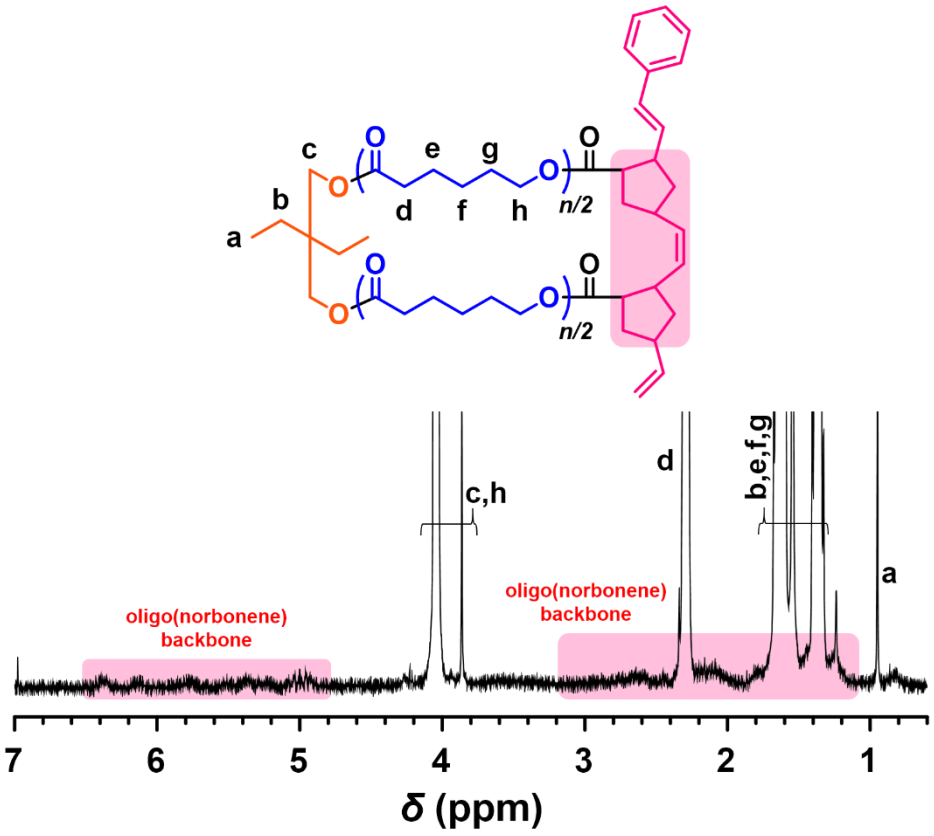


**Fig. S6** $^1$H NMR spectra of ***cy*-PCL$_{6k}$** in $CDCl_3$.

**Synthesis of *st*-PCL$_{9k}$.** Method A was used for the synthesis of ***st*-PCL$_{9k}$-OH** with ε-CL (3.00 g, 26.3 mmol) with trimethylolpropane (33.5 mg, 250 μmol) and DPP (6.30 mg, 252 μmol) at 80 °C for 250 min, giving ***st*-PCL$_{9k}$-OH** as a white solid (Scheme S3). Yield: 71.7%. $^1$H NMR (400 MHz, $CDCl_3$): $\delta$ (ppm) 4.13-4.01 (m, -OCO($CH_2$)$_4$C$H_2$-), 3.88 (s, ($CH_3CH_2$)$_2$C(C$H_2$O-)$_2$), 3.65 (q, $J$ = 6.4, -C$H_2$OH), 2.38-2.30 (m, -OCOC$H_2$($CH_2$)$_4$-), 1.75-1.54 (m, -OCOCH$_2$C$H_2$($CH_2$)$_3$-, -

OCO($CH_2$)$_3$C$H_2$C$H_2$-), 1.45-1.32 (-OCO($CH_2$)$_2$C$H_2$($CH_2$)$_2$-, -C$H_2$CH$_3$), 0.97 (t, -CH$_2$C$H_3$) (Figure S7). $M_{n,NMR}$ = 9,400 g mol$^{-1}$; $M_{n,SEC}$ = 14,600 g mol$^{-1}$; Đ = 1.06 (Figure S8).

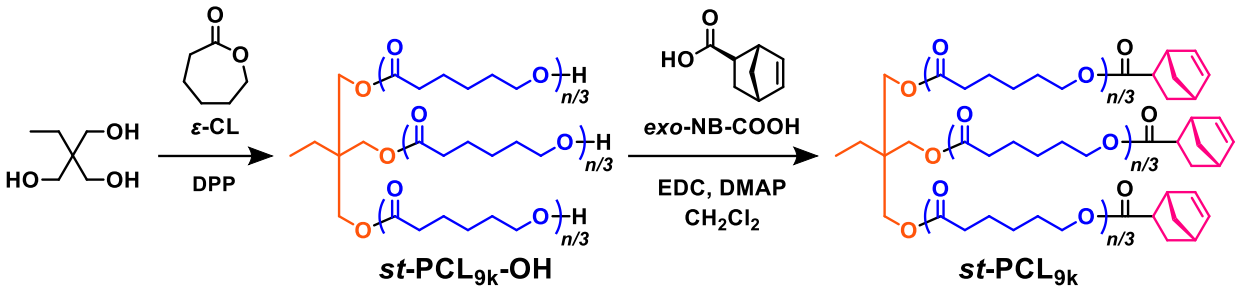


**Scheme S3.** The synthesis of *st*-PCL$_{9k}$, which is a star PCL based on one jointing point and three end groups capped with *exo*-NB-COOH.

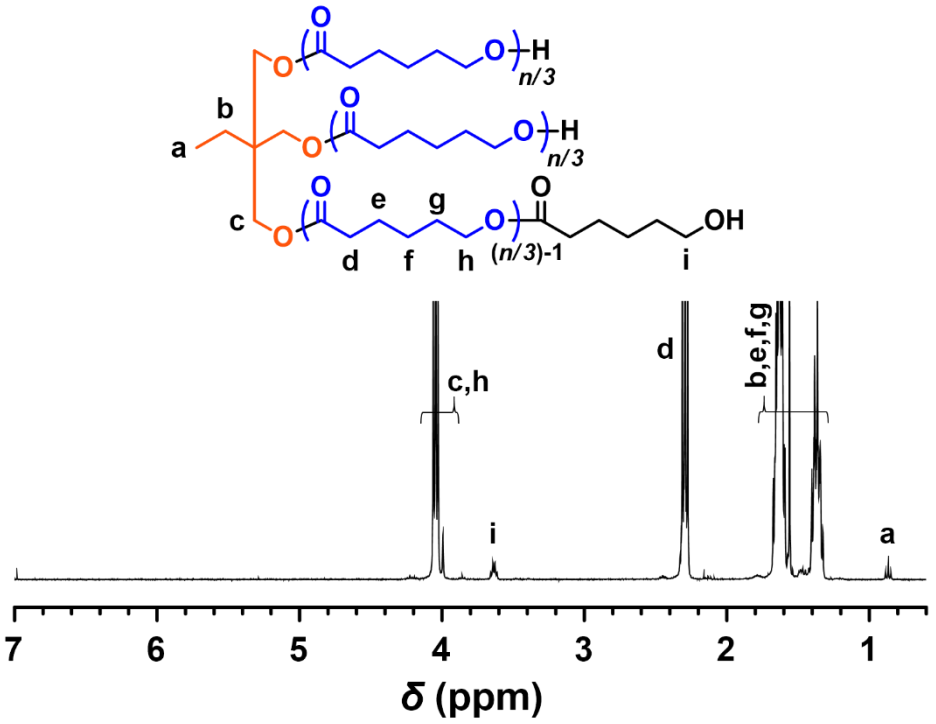


**Fig. S7** $^1$H NMR spectra of ***st*-PCL$_{9k}$-OH** in CDCl$_3$.

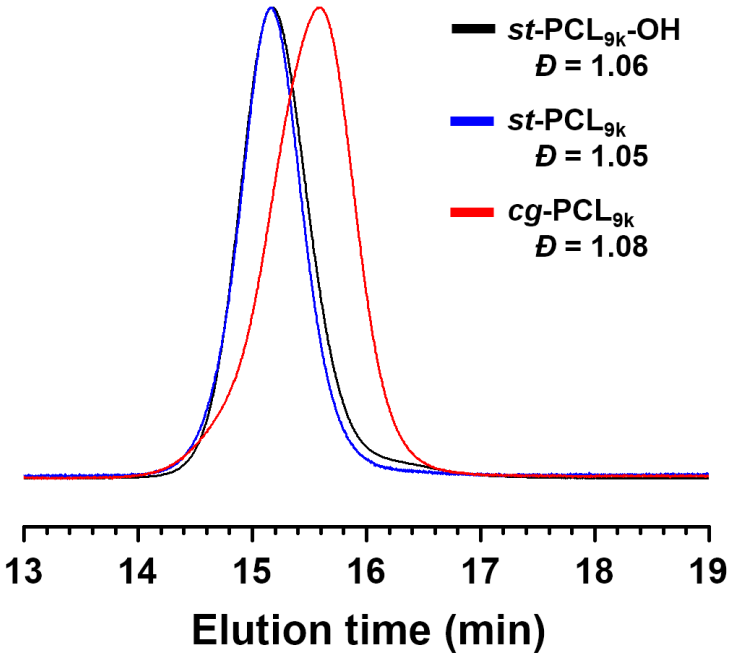


**Fig. S8** SEC traces of ***st*-PCL$_{9k}$-OH** (black), ***st*-PCL$_{9k}$** (blue), and ***cg*-PCL$_{9k}$** (red) in THF (RI detection; eluent, THF; flow rate, 1.0 mL min$^{-1}$; PSt standard).

The obtained ***st*-PCL$_{9k}$-OH** was subjected to $\omega$-end functionalization through Method B with **st-PCL$_{9k}$-OH** (1.50 g, 160 μmol), *exo*-NB-COOH (132 mg, 957 μmol), DMAP (175 mg, 1.44 mmol), and EDC (296 mg, 1.44 mmol) in $CH_2Cl_2$ (12 mL) (Scheme S3). The crude product was purified by reprecipitation from $CH_2Cl_2$ into cold methanol to give ***st*-PCL$_{9k}$** as a white solid. Yield: 56.8%. $^1$H NMR (400 MHz, $CDCl_3$): $\delta$ (ppm) 6.11 (m, -C*H*=C*H*- in norbornene ring), 4.09-4.02 (m, -OCO($CH_2$)$_4$C*H*$_2$-), 3.99 (s, ($CH_3CH_2$)$_2$C(C*H*$_2$O-)$_2$), 3.01 (s, -C*H*-CH-COO- in norbornene ring), 2.90 (s, -C*H*-$CH_2$-CH-COO- in norbornene ring), 2.35-2.25 (m, -OCOC*H*$_2$($CH_2$)$_4$-), 2.20 (m, -$CH_2$-C*H*-COO-), 1.89 (m, *exo*-C*H*- of -CH-C*H*$_2$-CH-COO- in norbornene ring), 1.80-1.50 (m, -OCOC$H_2$C*H*$_2$($CH_2$)$_3$-, -OCO($CH_2$)$_3$C*H*$_2$C$H_2$-), 1.47-1.30 (m, $CH_3$C*H*$_2$-, -OCO($CH_2$)$_2$C*H*$_2$($CH_2$)$_2$-, bridge head -$CH_2$- in norbornene ring, *endo*-C*H*- of -CH-C*H*$_2$-CH-COO-), 0.87 (s, C*H*$_3$$CH_2$-) (Figure S9). $M_{n,NMR}$ = 10,600 g mol$^{-1}$; $M_{n,SEC}$ = 14,700 g mol$^{-1}$; $Đ$ = 1.05 (Figure S8).

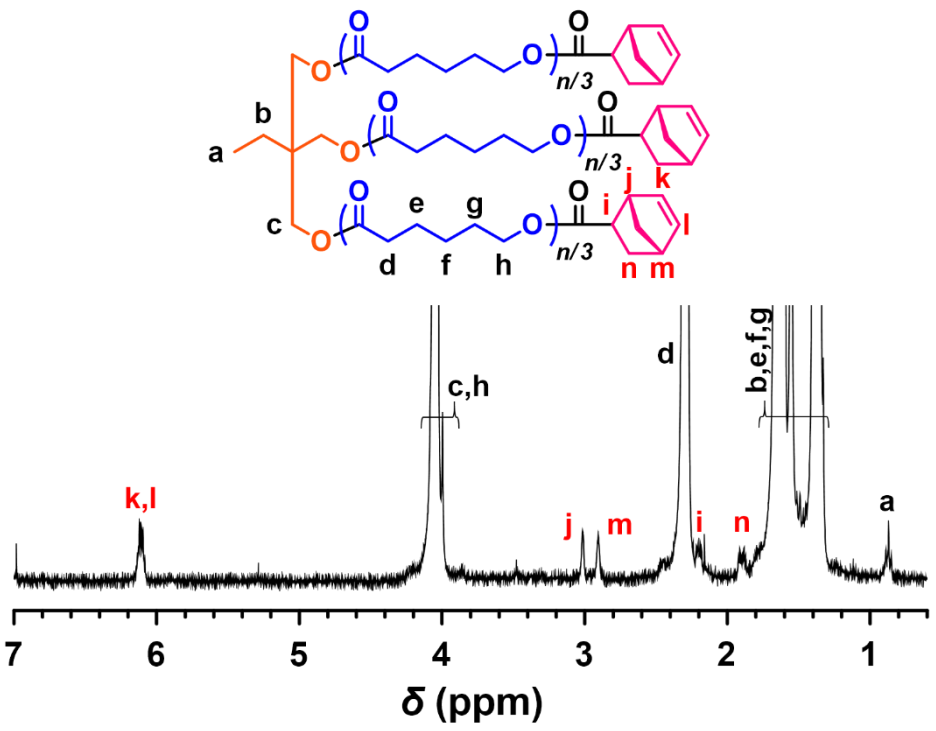


**Fig. S9** $^{1}$H NMR spectra of ***st*-PCL$_{9k}$** in $CDCl_3$.

**Synthesis of *cg*-PCL$_{9k}$.** Method C was used for the intramolecular cyclization of ***st*-PCL$_{9k}$** ($M_{n,NMR}$ = 10,600 g mol$^{-1}$, 110 mg, 10.3 μmol, 170 μM in $CH_2Cl_2$) with G3 (55.0 mg, 62.1 μmol) in $CH_2Cl_2$ (520 mL) to give ***cg*-PCL$_{9k}$** as a pale brown solid (Scheme S4). (74.5 mg) Yield: 67.7%. $^{1}$H NMR (400 MHz, $CDCl_3$): $\delta$ (ppm) 6.57-4.81 (br, alkenyl of poly(norbornene) backbone), 4.31-3.83 (m, -OCO($CH_2$)$_4$C$H_2$-, $CH_3C(CH_2O\text{-})_3$), 3.15-1.12 (br, cyclopentane ring of poly(norbornene) backbone), 2.51-2.20 (m, -OCOC$H_2$($CH_2$)$_4$-), 1.87-1.06 (m, -OCOCH$_2$C$H_2$($CH_2$)$_3$-, -OCO($CH_2$)$_3$C$H_2$C$H_2$-), 1.45-1.30 (m, $CH_3CH_2$-, -OCO($CH_2$)$_2$C$H_2$($CH_2$)$_2$-), 0.88 (t, $J$ = 7.5, C$H_3$CH$_2$-) (Figure S10). $M_{n,SEC}$ = 11,900 g mol$^{-1}$; $Đ$ = 1.08 (Figure S8).

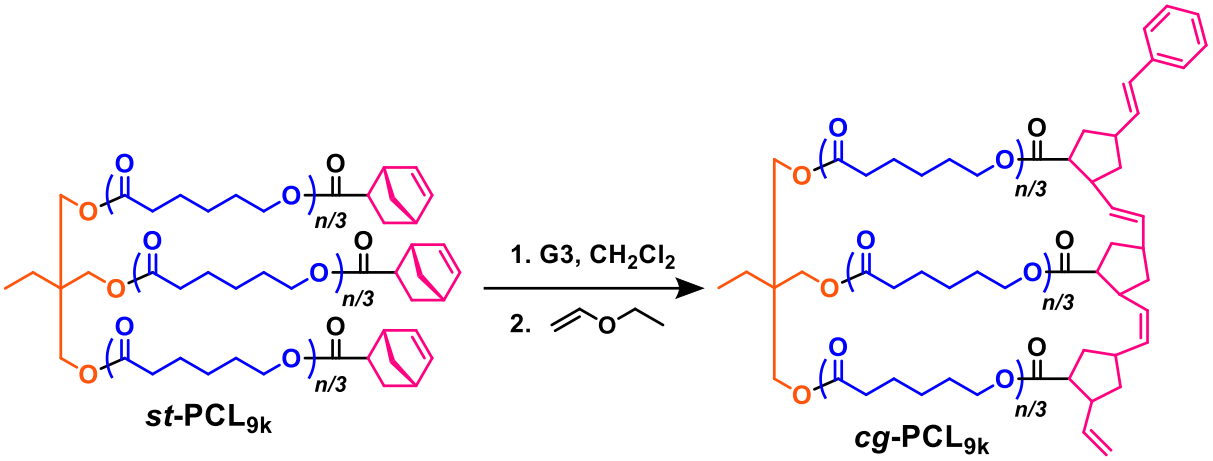


**Scheme S4.** The synthesis of ***cg*-PCL$_{9k}$** from ***st*-PCL$_{9k}$**.

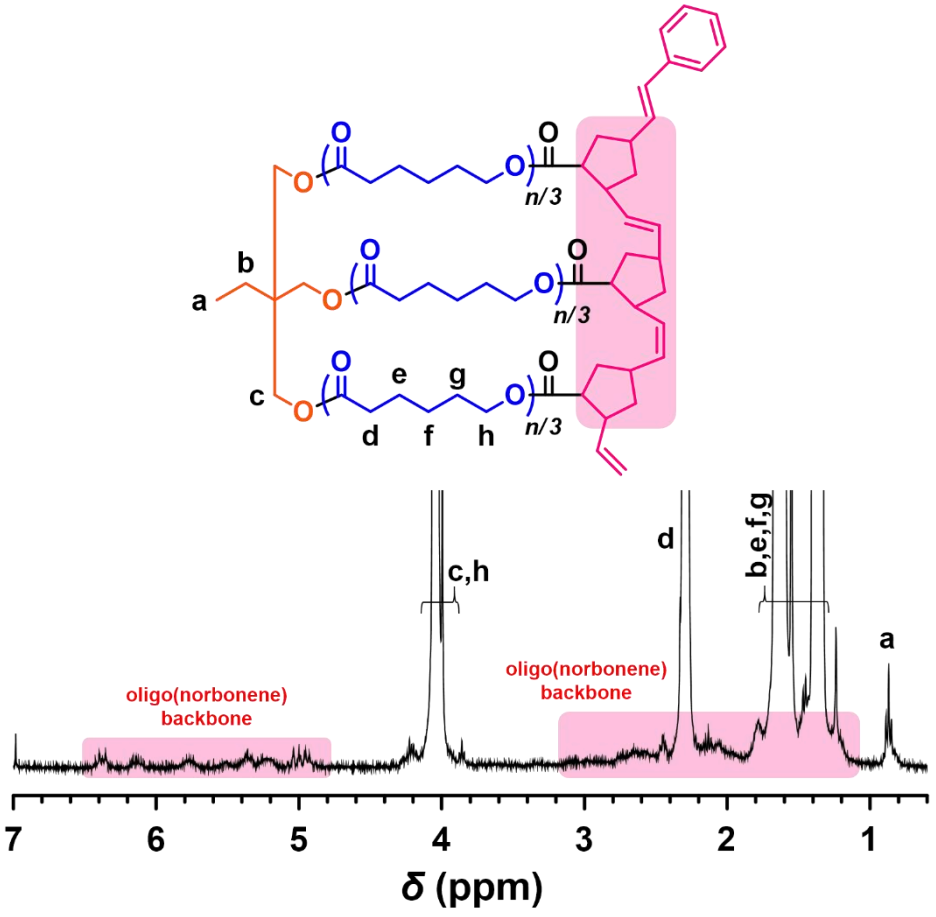


**Fig. S10** $^{1}$H NMR spectra of ***cg*-PCL$_{9k}$** in $CDCl_3$.

## References


(1) B. Lee, Y.-H. Park, Y. Hwang, W. Oh, J. Yoon and M. Ree, *Nat. Mater*., 2005, **4**, 147−150.

(2) B. Lee, J. Yoon, W. Oh, Y. Hwang, K. Heo, K. S. Jin, J. Kim, K.-W. Kim and M. Ree, *Macromolecules*, 2005, **39**, 3395−3405.

(3) B. Lee, I. Park, J. Yoon, S. Park, J. Kim, K.-W. Kim, T. Chang and M. Ree, *Macromolecules*, 2005, **38**, 4311−4323.

(4) S. Jin, J. Yoon, K. Heo, H.-W. Park, T. J. Shin, T. Chang and M. Ree, *J. Appl. Crystalogr*., 2007, **40**, 950−958.

(5) K. Heo, J. Yoon, S. Jin, J. Kim, K.-W. Kim, T. J. Shin, B. Chung, T. Chang and M. Ree, *J. Appl. Crystallog.*, 2008, **41**, 281−291.

(6) Y. Rho, B. Ahn, J. Yoon and M. Ree, *J. Appl. Crystallogr*., 2013, **46**, 466−475.

(7) M. Ree, *Macromol. Rapid Commun*., 2014, **35**, 930−959.

(8) *Methods of X-ray and Neutron Scattering in Polymer Science*, Y. J. Roe, New York: Oxford University Press, 2000.

(9) R. Lazzari, *J. Appl. Crystallogr*., 2002, **35**, 406−421.

(10) G. Renaud, R. Lazzari and F. Leroy, *Surf. Sci. Rep*., 2009, **64**, 255−380.

(11) J. S. Pedersen, *J. Appl. Crystallogr*., 1994, **27**, 595−608.

(12) *Direct analysis of diffraction by matter*, R. Hosemann and S. N. Bagchi, Amsterdam: North-Holland, 1962.

(13) G. Kim, J. Yoon, J.-S. Kim, H. Kim and M. Ree, *J. Phys. Chem. B*, 2008, **112**, 8868−8870.

(14) B. J. Ree, D. Aoki, J. Kim, T. Satoh, T. Takata and M. Ree, *Macromolecules*, 2019, **52**, 5325−5336.

(15) B. J. Ree, D. Aoki, J. Kim, T. Satoh, T. Takata and M. Ree, *Macromol. Rapid Commun*., 2019, **40**, 1900334.

(16) J. Yoon, K. S. Jin, H. C. Kim, G. Kim, K. Heo, S. Jin, J. Kim, K.-W. Kim and M. Ree, *J. Appl. Crystallogr*., 2007, **40**, 476−488.

(17) Y. Rho, J. Min, J. Yoon, B. Ahn, S. Jung, K. Kim, P. Shah, J.-S. Lee and M. Ree, *NPG Asia Mater*., 2012, **4**, e29.

(18) B. Ahn, D. M. Kim, J.-C. Hsu, Y.-G. Ko, T. J. Shin, J. Kim, W.-C. Chen and M. Ree, *ACS Macro Lett.*, 2013, **2**, 555−560.

(19) S. G. Hahm, Y. Rho, J. Jung, S. H. Kim, T. Sajoto, F. S. Kim, S. Barlow, C. E. Park, S. A. Jenekhe, S. R. Marder and M. Ree, *Adv. Funct. Mater*., 2013, **23**, 2060−2071.

(20) M. Matsuo, M. Tamada, T. Terada, C. Sawatari and M. Niwa, *Macromolecules*, 1982, **15**, 988−988.

(21) Y. Mato, K. Honda, K. Tajima, T. Yamamoto, T. Isono and T. Satoh, *Chem. Sci*., 2019, **10**, 440-446.

(22) M. Ouchi, Y. Inoue, K. Wada, S. I. Iketani, T. Hakushi and E. Weber, *J. Org. Chem*., 1987, **52**, 2420-2427.